ORIGINAL ARTICLE



Three-dimensional perspective on a convective instability and transition to turbulence in an internal solitary wave of depression shoaling over gentle slopes

Gustavo Rivera-Rosario¹ · Peter J. Diamessis¹ · Ren-Chieh Lien² · Kevin G. Lamb³ · Greg N. Thomsen⁴

Received: 9 July 2021 / Accepted: 13 February 2022 © The Author(s), under exclusive licence to Springer Nature B.V. 2022

Abstract

The shoaling of an internal solitary wave (ISW) of depression is explored in three-dimensions (3D) through high-accuracy, fully nonlinear, and nonhydrostatic simulations. Timeaveraged background stratification and current profiles from field observations, along with measured bathymetry data from the South China Sea (SCS), are used. The computational approach is based on a high-resolution and high-accuracy deformed spectral multidomain penalty method incompressible flow solver. Recent field observations in the SCS indicate the presence of a convective instability followed by a subsurface recirculating core that may persist for more than tens of km and drive turbulent-induced mixing, estimated to be up to four orders of magnitude larger than that typically found in the ocean. The preceding convective instability occurs due to a sudden decrease in the wave propagation speed, below the maximum horizontal wave-induced velocity, and possible from the stretching of the near-surface vorticity layer of the baroclinic background current from the propagating ISW. Motivated by such observations, the present study examines the onset of the 3D convective instability that results in subsurface recirculating core formation, as the ISW propagates and shoals in the normal-to-isobath direction. A noise field is inserted in the wave-induced velocity and density field to force the evolution in 3D. The initial instability has a transitional structure that develops in the lateral direction. The evolution of the lateral instability and subsequent transition to turbulence in the breaking wave is compared with the wave structured observed in the field. As such, a preliminary understanding of the formation of recirculating cores in ISWs, the driver for subsequent turbulence, mixing, and particle transport in the interior is obtained.

Keywords Internal solitary waves (ISW) of depression · Convective instability · Subsurface recirculating core

Published online: 04 March 2022



[☐] Gustavo Rivera-Rosario gr327@cornell.edu

School of Civil and Environmental Engineering, Cornell University, Ithaca, NY, USA

Applied Physics Laboratory, University of Washington, Seattle, WA, USA

Department of Applied Mathematics, University of Waterloo, Waterloo, ON, Canada

Wandering Wakhs Research, Austin, TX, USA

1 Introduction

Internal solitary waves (ISW) of depression in the ocean, characterized by their large displacement of the pycnocline, have been observed to become unstable as they propagate over gentle slopes [1–5]. An unstable ISW dissipates its kinetic energy, through turbulence caused by shear and convective instabilities thereby enhancing fluid mixing, and may transport suspended material across significant distances [6]. The wave also interacts with the bottom by inducing effective boundary layer separation in the adverse pressure gradient region in the rear of the wave, that may be strong enough to produce vortex shedding and a near-bed turbulent wake and impact the bed [7–12].

In regards to turbulence produced by shear or convective instabilities in the ISW interior, a small number of direct in situ measurements of ISW shear instabilities in the oceanic thermocline have been reported in the past 20 years. Enhanced turbulent mixing has often been observed in acoustic backscatter and microstructure profilers measurements through ISWs believed to be subject to strong shear instability [5, 13–15]. Similarly, more recent observations of shear instability in ISWs have also been conducted by Chang et al. [1] using Acoustic Doppler Current Profilers (ADCPs) and high-frequency sampling thermistor chains. Shroyer et al. [16] reported that during low-wind conditions ISW trains on the New Jersey continental shelf contribute to nearly 50% of the total heat flux across the thermocline (see their Figs. 1 and 2) and non-trivial mass transport. The average turbulent heat flux across the pycnocline is about 800 W m⁻², similar to that observed on the Oregon shelf by Moum et al. [5].

When an ISW shoals over gentle slopes (i.e. less than 0.03), the propagation speed may decrease below the wave-induced horizontal velocity and cause a sudden steepening at the rear, as proposed by the model configuration of Vlasenko et al. [17]. As a result, there is an intrusion of heavy fluid that rises from the lower layer of the water column into the region above the wave trough where lighter fluid resides. This heavy-over-light configuration is convectively unstable leading to enhancement of turbulent mixing and energy dissipation. Additionally, as the ISW shoals and becomes unstable, a region of closed streamlines may develop inside the wave where fluid is transported with the wave, if there is a pre-existing background vorticity at the top of the water column. This region is typically regarded as a recirculating, or trapped, core [18–20]. The near-surface vorticity may originate from either the background density profile or a background current profile possibly associated with the internal tide. Without background vorticity, the ISW can become convectively unstable but no core will form [20, 21].

Most laboratory experiments, simulations, and field work have highlighted the existence and properties of ISWs with cores that are located near the surface of the water column. However, the recent observations from Lien et al. [3, 4] indicated the presence of *subsurface* cores, located closer to the ISW trough. They reported turbulent vertical diffusivity in the 50–100 m tall recirculating core as 0.1-1 m² s⁻¹, estimated crudely using the Thorpe scale and background stratification. The estimated turbulent heat flux in the convective core was $\mathcal{O}(10^4-10^5)$ W m⁻², approximately 100 times greater than that of shear-breaking ISWs observed by Shroyer co-workers on the New Jersey shelf. The mass transport per unit wave crest length was estimated as more than 100 times larger than calculated on the New Jersey shelf.

What dictates whether the core resides closer to either the free-surface or the ISW wave trough is the sign of the pre-existing background vorticity in the water column that is linked to the baroclinic background current. Using a two-layer stratified water column, Choi [22]



originally examined the core location by comparing against the background water column properties, and concluded that if upper layer vorticity is of the same sign as the vorticity associated with the ISW then a core will form at the surface. On the other hand, if the vorticity is opposite in sign then a subsurface core will form. Their conclusions were recently corroborated through the numerical 2D study of He et al. [23] that simulated ISWs of depression shoaling over an idealized bathymetry. Subsequent work by Rivera-Rosario et al. [24] considered the recorded background water column properties and bathymetry from Lien et al. [4] and also captured a subsurface recirculating core in a shoaling ISW of depression over a gentle slope. Their study was based on highly-accurate numerical simulations in 2D that also explored the preceding convective instability.

The work of Lien et al. [3, 4] detailed the only known observations of ISWs with subsurface cores, and their unique impact on the water column through the use of shipboard measurements and data from two moorings deployed 6 km apart on the Dongsha Slope in the SCS. Analysis of long-term observations by Chang et al. [1] and more recent observations by Chang et al. [2] further noted the presence of a convectively breaking ISW of depression shoaling near the Dongsha Slope in the SCS. They considered the turbulent aspect of the ensuing core, but did not indicate whether it was a subsurface or surface core. It is possible that they were in fact observing an ISW with a subsurface core. The Dongsha slope in the SCS is the only location in the world where ISWs of depression with subsurface cores have been observed, and it may be possible that waves with subsurface cores exists in other regions that share similar water column properties.

A large sample of the ISWs observed by Chang et al. [2] were regarded by the authors as having a *marginal convective instability* status such that (1) the maximum current speed remains nearly equal to the propagation speed and (2) for large-amplitude convectively breaking waves the current speed and propagation speed decrease at nearly the same rate over a long distance. They concluded that the marginal convective instability occurs because ISWs adjust gradually to the gently sloping bottom and preserve their structural integrity after the onset of breaking. The earlier numerical work of Rivera-Rosario et al. [24] examined the effects of the gently varying bathymetry and core formation in 2D, yet no context can be inferred on the formation of a marginal convective instability in a shoaling ISW. Examining how the breaking process also evolves in 3D is key in shedding context on the field observations of both Lien et al. [3, 4] and Chang et al. [1, 2].

Studies of convectively unstable and linear interfacial waves in 3D have highlighted the excitation of higher modes during the breaking process [25] and the emergence of secondary, spanwise structures that generate potential vorticity [26]. These structures contribute to the development of finer motion, and ultimately turbulence, that leads to mixing and dissipation [27-29]. However, no known work has examined the 3D nature of convective breaking for highly nonlinear ISWs of depression, similar to those observed in the SCS, including the formation of a subsurface recirculating core. To this end, highly accurate numerical simulations can be utilized to capture the broad range of scales describing the phenomenology, such as the actual wave and gently varying water depth along with the core and, potentially, the small scale features throughout. The complex interplay involving the stratification, background current and density, and the gently varying bathymetry over long propagation distances calls for a numerical approach to examine the problem. The ISW is large and the core's lifespan occurs over long distances (i.e. $\mathcal{O}(km)$) and timescales of $\mathcal{O}(\text{hour})$ to $\mathcal{O}(\text{days})$, so field instruments would need to cover large ocean swaths for a prolonged period of time becoming potentially expensive or impractical to deploy. An accurate numerical study, guided by the obtained field observations, provides a sensible



approach to describe the convectively unstable ISW with the ensuing subsurface core formation in 3D.

To simulate the shoaling ISW, the spectral multidomain penalty method (SMPM), originally developed for the study of turbulent wakes in stratified flows by Diamessis et al. [30], can be adapted to incorporate high-order polynomial interpolation for representation of complex boundaries [31], thereby allowing use of an observed bathymetric profile. By utilizing a high-order approach, a lower number of grid points is needed to resolve the wave propagation with minimal numerical diffusion and dispersion compared to traditional low-order schemes [32]. In addition, the multidomain aspect allows for resolution to be localized at regions of interest throughout the domain. The adapted SMPM method was successfully utilized by Rivera-Rosario et al. [24] to simulate ISWs of depression that became convectively unstable and developed a subsurface recirculating core in 2D. The method has been extended to include a third, spanwise or lateral direction with a Fourier expansion, making it ideal for simulating normal-to-isobath wave propagation in 2D and capturing any 3D transition to turbulence as a result of wave breaking.

Motivated by the field observations of Lien et al. [3, 4] and 2D simulations of subsurface cores in shoaling ISWs over gentle slopes, this study examines the shoaling of an ISW of depression in 3D by utilizing field observations to generate the initial conditions corresponding to the ISW-induced velocity and density field and then simulating wave propagation over realistic bathymetry. The simulation builds on Rivera-Rosario et al. [24], by utilizing their baseline ISW, with an initial amplitude of 143 m, along with the observed background density and current profiles from June 2, 2011 from Lien et al. [4], in addition to the measured SCS bathymetric profile. The ISW is modeled in 3D as it becomes convectively unstable and shoals over the steepest portion of the bathymetric transect, where the field data confirms the presence of a subsurface recirculating core. To achieve 3D breaking, noise is inserted in the wave-induced velocity and density. Turbulent quantities such as dissipation of kinetic energy, mixing in the water column, and mass transport are not computed, as these will be the focus of a separate study on the 3D dynamics of the subsurface recirculating core itself. The present work aims to capture the process by which wave breaking transitions from 2D to 3D and results in core formation.

To this end, the following questions guide the present study: (a) is the expected convective instability predominantly 2D?, and (b) how does the evolution of the gravest lateral instability mode compare with the development of the primary convective overturn? The primary objective of this paper to establish a robust high-accuracy and high-resolution simulation-based framework which can model, in three-dimensions: (a) the development of convective instability and (b) the subsequent emergence of more complex chaotic motions in the wave interior, in the form of transition to turbulence, for an ISW shoaling over gentle slopes in a manner that is as consistent as possible with the observations of Lien et al. [3, 4]. The findings of this study will serve as the springboard for even higher-resolution future work of convectively breaking shoaling ISWs which capture both the resulting turbulence in the wave interior and the associated Lagrangian particle transport.

The work contained in this study is presented as follows: Sect. 2 discusses the methodology which includes the problem geometry, governing equations, and simulation description. Section 3 covers the results of the study by presenting isosurface visualizations, evolution of the 2D convective instability that forms, the wave properties in 2D and 3D, and the evolution of the lateral instability that drives 3D breaking. Concluding remarks and a short description of future work are included in Sect. 4.



2 Methodology

2.1 Problem geometry

The field data from Lien et al. [4] is used to generate the initial ISW-induced velocity and density perturbation from the solution of the DJL equation [33] and to also supply the background water column properties of the computational domain. The SCS gently varying bathymetry near the Dongsha Slope is also utilized; it spans from 21.07° N, 118.498° E to 21.0° N, 116.508° E, or approximately 200 km when converted to UTM. This bathymetry was recorded in 2005 by co-author Lien and the rest of the deployment team, and is presented in Lien et al. [3].

Rather than utilizing the 200 km-long ship-board recorded bathymetry to simulate the shoaling ISW, the reduced coordinates utilized by Rivera-Rosario et al. [24], that range from 21.07° N, 117.8° E to 21.07° N, 117.0° E, are used instead. This reduced bathymetric transect extends approximately over 80 km and contains the steepest portion where the slope reaches a value of 0.028, along with the location of the deployed subsurface and surface mooring from Lien et al. [4]. The mooring coordinates were 21.07° N, 117.27° E and 21.07° N, 117.22° E, respectively, and anchored at a water depth of 525 m and 450 m. These were used to record the water column temperature, density, and velocity during the expedition. To avoid ambiguity, these moorings are herein referred to as *deep* and *shallow*, respectively.

Figure 1 shows a diagram of the ISW shoaling problem setup. In Fig. 1a, the stratification is denoted by three grey-solid lines with the ISW indicated by the downward isopycnal displacement, in 2D. The wave propagates over a domain that has a length L_x , and a depth H(x). Figure 1b illustrates the domain in 3D, with the third dimension having a span of L_y . Figure 1c shows the ISW over a flat surface, along with the following wave properties: amplitude A, width L_w , and a propagation speed c. The wave amplitude is defined as the maximum isopycnal displacement, from the reference, unperturbed state. The wave width is the integral of the pycnocline displacement, in the along-wave direction [34] divided by the amplitude; it can be expressed as,

$$L_{w} = \frac{1}{A} \int_{-\infty}^{+\infty} \eta(x) dx, \tag{1}$$

where $\eta(x)$ is the isopycnal displacement for a given density value. In Fig. 1, the coordinate system is placed at the water surface, where z = 0. The along-wave, streamwise, direction is the positive x-direction, oriented towards the shallower water depth. This configuration is opposite to that from [4] where the eastward direction (towards deeper water) was taken to be positive.

In addition to the wave properties, adjusted time-averaged profiles of the measured background density, $\rho_o + \rho(z)$, the Brunt-Väisälä frequency, $N^2(z)$, the background current, U(z), and the background shear, $U_z(z)$, are also included in Fig. 1c. These profiles correspond to the state of the water column on June 2 from Lien et al. [4], prior to the arrival of the first ISW with a subsurface trapped core, and were measured through the deployed moorings. That day, the pycnocline was at $z_o = -22$ m, with a reference density of $\rho_o = 1026.58$ kg m⁻³. In the present study, the measured background current is smoothed to zero below 300 m such that no potential hydraulic effects through interactions with the



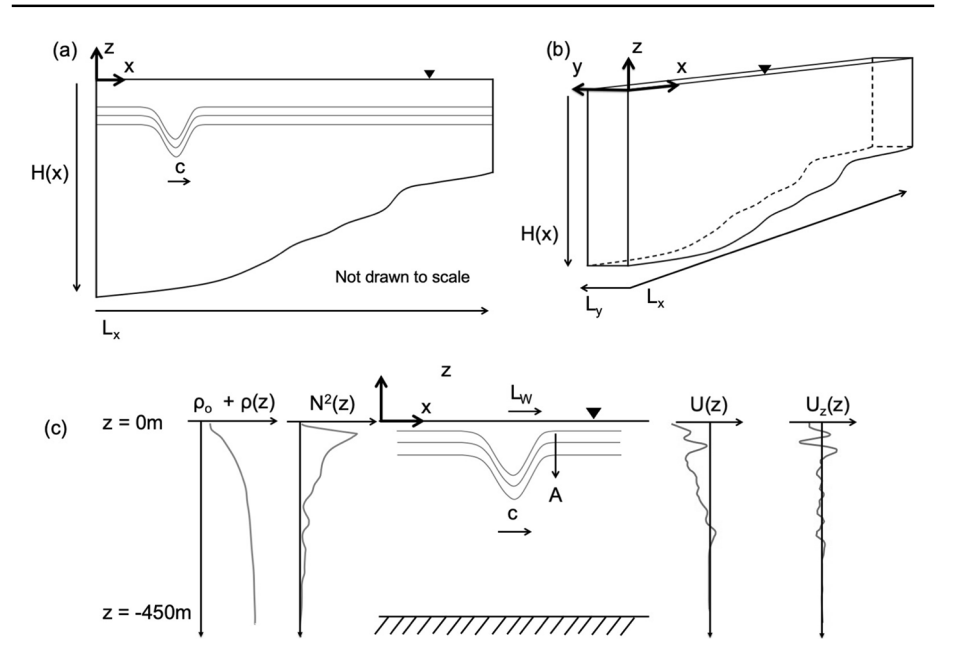


Fig. 1 Schematic of the shoaling problem for an internal solitary wave of depression. The 2D bathymetric transect is presented in **a**. Panel **b** shows the computational domain in 3D and panel **c** shows the initial wave and its properties. The shown wave properties are: width, L_w ; amplitude, A; and propagation speed, c. The reference datum is placed at the free-surface. The computational domain has a length, L_x , a span, L_y , and a variable depth, H(x). In **c**, the time-averaged background density profile, $\rho_o + \rho(z)$, and the Brunt-Väisälä frequency, $N^2(z)$, are denoted as the grey-solid line, while the time-averaged velocity profile, U(z), and background shear, $U_z(z)$, are shown as the solid-blue line. All background profiles are from the recorded data of Lien et al. [4]

varying bathymetry develop. Furthermore, the background current profile had to be linearly extrapolated near the top of the water column since the field observations did not cover the upper 10 m. Extrapolation is assumed to be linear because the resulting vorticity is negative at this region and this configuration is needed for subsurface cores to form [22, 23]. The choice of extrapolation was further discussed by Rivera-Rosario et al. [24].

To utilize the 3D variant of the adapted SMPM method [31, 35], no lateral variations in depth can be included in the computational domain given that the numerical scheme leverages a Fourier modal expansion in L_y [36]. Nonetheless, the field observations from Lien et al. [3, 4] indicated that the ISWs with subsurface recirculating cores propagated predominantly in a westward direction during shoaling. Since these waves propagate perpendicular to isobaths, it may be reasonable to assume that lateral variations in depth can be neglected. The SCS bathymetry is not necesarily constant in the longitudinal, or lateral, direction (see Fig. 1 of Lien et al. [3]). However, in the present study, the domain span is: (a) much smaller than the domain length; (b) assumed to be comparable to the observed wave amplitude; and (c) large enough such that at least two wavelengths of the primary spanwise instability can fit within it. The choice of domain span is covered in the following subsection.



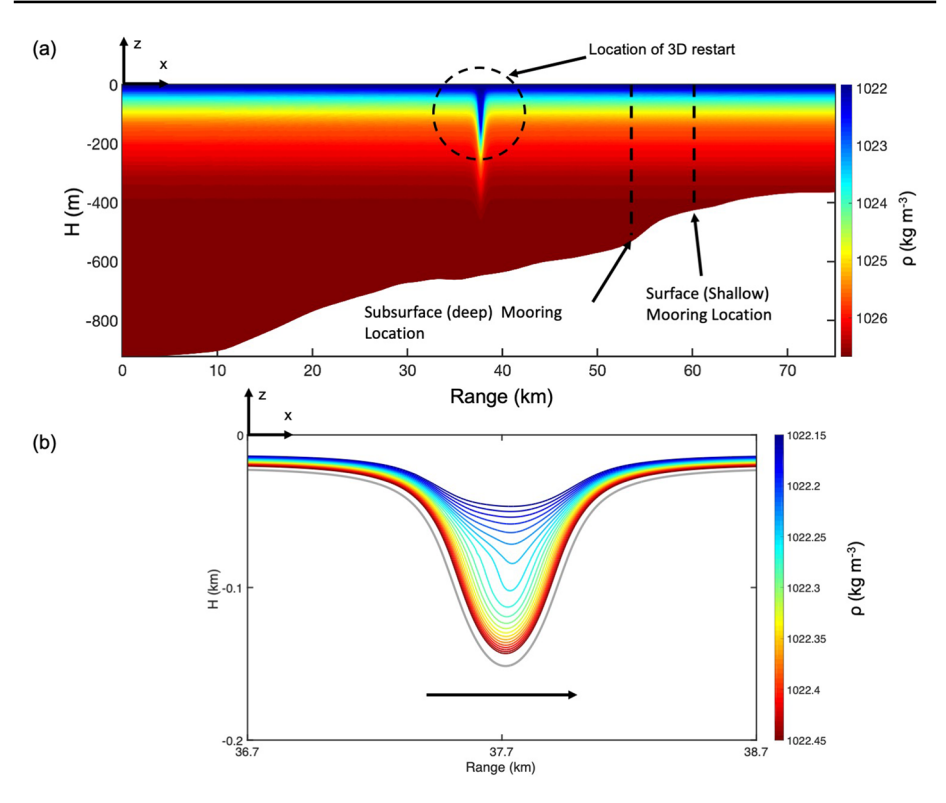


Fig. 2 SCS bathymetric transect with ISW at the location of the 3D restart. In **a**, the ISW is shown over the SCS transect along with the location of the subsurface (deep) and surface (shallow) mooring location as the black-dashed lines. In **b**, the ISW isopycnal strucutre above the pycnocline is shown, with the pycnocline denoted as the grey-solid line. In both **a** and **b** the contour variable is the total density field comprised of the superposition of the reference density, steady background density, and the wave-induced density perturbation

2.2 Simulation setup

2.2.1 Governing equations

The governing equations for the present simulation are the incompressible Navier–Stokes equations under the Boussinesq approximation (INSB) without rotation [37]. The velocity and density field are decomposed into a perturbation and a mean quantity, denoted by a prime and an overline respectively. The perturbation fields are taken to be the wave-induced velocity and density field, and the mean quantities the background current and density. The background fields are mainly driven by the internal tides which propagate at similar speeds as the internal solitary waves, and therefore both background velocity and density fields are assumed to be steady in time. The background density and velocity profiles from June 2 [4] were obtained from the deployed moorings, anchored at a fixed location and water depth. Given that there were no other measures of the water properties anywhere else along the transect, in the absence of any ISW, these recorded profiles are then assumed to be homogeneous in the lateral and along the direction of propagation in the present study.



In vector form, for a fixed reference frame without rotation, the mass conservation and momentum equations are:

$$\nabla \cdot \mathbf{u} = 0 \tag{2}$$

$$\frac{\partial u'}{\partial t} + u' \frac{\partial u'}{\partial x} + v' \frac{\partial u'}{\partial y} + w' \frac{\partial u'}{\partial z} = -\frac{1}{\rho_0} \frac{\partial p'}{\partial x} - U \frac{\partial u'}{\partial x} - w' \frac{\partial U}{\partial z} + v \nabla^2 u', \tag{3}$$

in the along-wave, x, direction,

$$\frac{\partial v'}{\partial t} + u' \frac{\partial v'}{\partial x} + v' \frac{\partial v'}{\partial y} + w' \frac{\partial v'}{\partial z} = -\frac{1}{\rho_o} \frac{\partial p'}{\partial y} - U \frac{\partial v'}{\partial x} + v \nabla^2 v', \tag{4}$$

in the lateral, y, direction, and

$$\frac{\partial w'}{\partial t} + u' \frac{\partial w'}{\partial x} + v' \frac{\partial w'}{\partial y} + w' \frac{\partial w'}{\partial z} = -\frac{1}{\rho_o} \frac{\partial p'}{\partial z} - U \frac{\partial w'}{\partial x} + v \nabla^2 w' - \frac{\rho' g}{\rho_o}, \tag{5}$$

in the vertical z direction. Here, \mathbf{u} is the three-dimensional velocity field (i.e. $\mathbf{u} = (u' + U, v', w')$) with U = U(z), p'(x, y, z, t) is the perturbation pressure with respect to the reference background state, t is time, v is the kinematic viscosity, and g is the gravitational acceleration; the Earth's rotation is neglected. During shoaling, the effects of changing water depth may dominate over rotational forces [38]. Nevertheless, rotation results in radiation of long inertia-gravity waves which decreases ISW amplitudes over longer time scales than considered here [38, 39].

The density equation is given as,

$$\frac{\partial \rho'}{\partial t} + \nabla \cdot \left[\mathbf{u} \left(\rho' + \overline{\rho}(z) \right) \right] = \kappa \nabla^2 \rho', \tag{6}$$

where κ is the mass diffusivity. In Eqs. (3–6), the diffusion of the background profiles is neglected. Similar to [24], the present study uses a Reynolds number of $Re = c_i H_i / v = 2 \times 10^6$ and a Schmidt number of Sc = 1. Here, c_i and H_i are the initial wave propagation speed and water column depth. Both Re and Sc are two orders of magnitude below those observed by Lien et al. [4] yet were proven to not suppress the formation of the convective instability which is the primary instability and always precedes subsurface core formation. Lastly, following the Boussinesq approximation, the reference pressure, $\overline{p}(z)$, is in hydrostatic balance with the background field in the absence of any wave propagation:

$$\frac{\partial \overline{p}}{\partial z} = -(\rho_o + \overline{\rho})g. \tag{7}$$

2.2.2 Numerical method

The INSB are decomposed into a perturbation and a steady field that can be solved numerically via the 3D deformed-domain variant of the spectral multidomain penalty method (SMPM) [31]; it is collocation-based in the x and z direction and equidistant in the y direction. A local Legendre-polynomial expansion is used to approximate the solution at each node of a Gauss-Lobatto-Legendre (GLL) grid in each element [36]. The velocity and density fields are expanded with Fourier basis function in the lateral. Periodicity can be



used across the transect, in the y direction, by assuming no lateral depth variations. Time-integration is achieved via a stiffly-stable third order scheme [40].

The boundary conditions, used to solve the momentum equations of the INSB are set as free-slip/no-flux at all four physical boundaries and periodic in the lateral direction. In addition, at the left and right boundaries of the computational domain, an artificial Rayleigh-type damper, one ISW-width thick, is applied to eliminate any possible reflection from the incoming ISW [41]. For the density equation of the INSB, no-flux boundary conditions are implemented in all four physical boundaries, along with the Rayleigh-type damper at the left and right boundary. Lastly, an exponential spectral filtering technique is applied in all directions to dissipate any numerical instabilities due to underresolution [42, 43]. This filtering process is applied three times per time-step.

2.2.3 Problem configuration

To construct the computational domain, the latitude and longitude coordinates of the shortened transect given in Sect. 2.2.1 were converted to UTM. The resulting conversion yielded a transect that is approximately $L_x = 80$ km long, with the deepest and shallowest depth being 921 m and 360 m, respectively. The deepest point of the 2D transect was then used, along with the observed background density profile and modified background current profile (see Sect. 2.2.1), to generate the initial conditions representing the ISW obtained from the solution of the DJL equation [44, 45], using the nonlinear eigenvalue solver of Dunphy et al. [33] over a flat domain. The obtained ISW had an initial amplitude of $A_i = 143$ m, a width of $L_{w,i} = 1014$ m, and a propagation speed of $c_i = 1.92$ m s⁻¹, the same initial baseline wave used by Rivera-Rosario et al. [24]. The wave-induced fields were then interpolated onto the SMPM grid using cubic splines and placed onto a constant-depth region of 921 m-deep and 20 km-long that is added to the SCS bathymetric transect prior to the start (see Fig. 3 of Rivera-Rosario et al. [24]). This constant depth start-up procedure allows the wave to propagate without inducing shoaling prior to encountering the varying depth.

To numerically solve Eqs. (3–6) with the SMPM flow solver, the computational domain is partitioned into m_x subdomains in the horizontal and m_z subdomains in the vertical direction, with n points per subdomain in each direction. In the lateral direction, the number of points is denoted as m_y . The total number of degrees of freedom for the entire computational domain is defined as $n^2m_xm_zm_y$. However, a window technique is employed to drastically reduce the number of actively simulated degrees of freedom at any given time; it is further explained in the subsequent paragraphs. The number of subdomains in the horizontal is set to 1600 and the number of subdomains in the vertical is $m_z = 25$. The number of points per subdomain is constant in both directions, at n = 15. The subdomains are uniformly spaced in the n_x and n_y -direction, and account for the deformation of the bathymetry. Lastly, the exponential filter order used in the horizontal, vertical, and lateral directions is set to 11, which is the optimal choice to preserve numerical stability [30, 42, 46].

Two strategies are employed to reduce the computational cost per timestep: (1) an initial 2D simulation with a subsequent 3D restart and, (2) a partition of the computational domain into overlapping windows that track the wave as it shoals. As a result, the total number of actively simulated degrees of freedoms will be much less than n^2m_x m_zm_y. First, the shoaling simulation is initialized in 2D, with the ISW propagating for approximately 40 km after the start of the transect and prior to becoming convectively



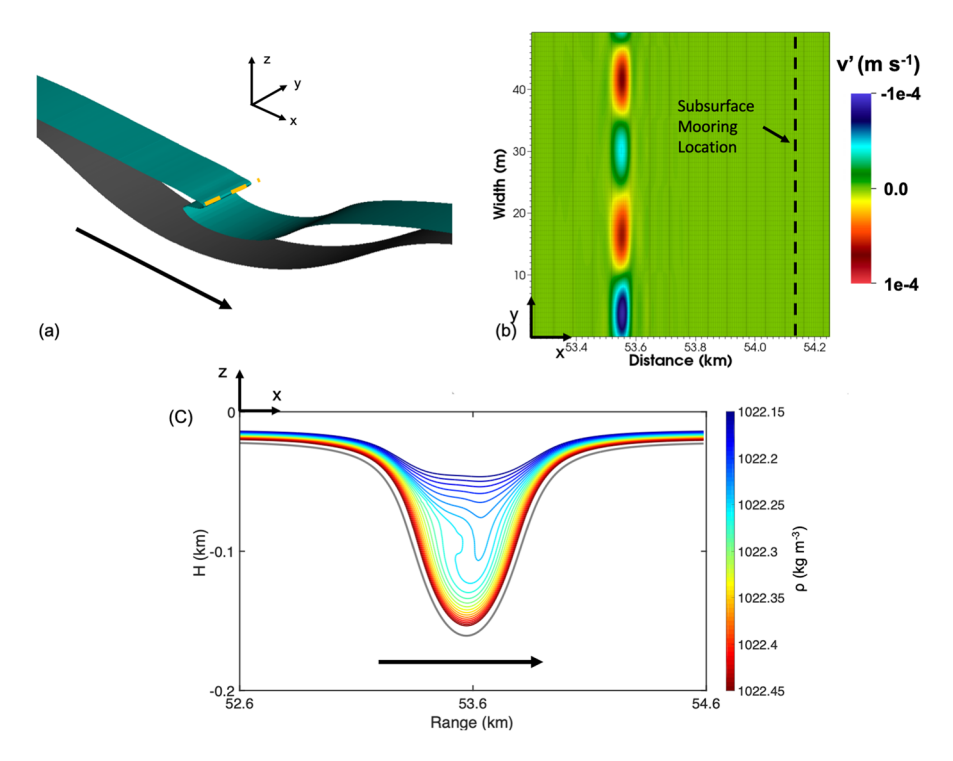


Fig. 3 ISW close to the deep mooring location. In **a**, two density isosurfaces of the ISW are shown: $\rho_c = 1022.26 \text{ kg m}^{-3}$ (cyan) and $\rho_o 1022.58 \text{ kg m}^{-3}$ (grey). The black arrow indicates the direction of wave propagation. The orange-dashed line denotes the 2D convective instability $U_{max} > c$, at an approximate depth of 100 m. In **b**, a horizontal plane transect in the x-y direction at the depth of 100 m has been extracted and is shown with the lateral wave-induced velocity, v', as the contour variable to visualize the lateral instability. The plane cuts through the ρ_c isosurface seen in **a**. The location of the deep mooring is denoted by the black-dashed line. In **c**, a lateral plane transect in the x-z direction with the isopycnal structure above the pycnocline is shown. The x-z cut-plane was extracted at span of approximately y=25 m. The pycnocline is denoted as the grey-solid line. The black arrow denotes the direction of propagation

unstable. Rivera-Rosario et al. [24] indicated that the propagation speed of the 2D ISW should drop below U_{max} shortly thereafter. The 2D simulation is then stopped, and the computational domain is then extruded in the lateral direction using the chosen values of m_y and L_y . The simulation is subsequently restarted in 3D and the wave continues to propagate towards shallower water.

Figure 2 shows the ISW over the SCS bathymetric transect at the location where the 3D restart occurs. In Fig. 2a, the ISW is included along with the location of the moorings, denoted by the black-dashed lines. In Fig. 2b, the interior isopycnal structure above the pycnocline is shown. Here, the pycnocline is denoted by the grey-solid line and the arrow denotes the direction of propagation. In both Fig. 2a and b, the contour variable is the total density: $\rho_o + \overline{\rho} + \rho'$. After the 3D restart, the ISW continues to propagate towards the moorings and the shallower water of the transect.

The second strategy to accelerate the simulation in the present study involves partitioning the computational domain into overlapping windows of approximately $16L_{w,i}$ with an overlapping length between 6 and $7L_{w,i}$, depending on the ISW location and propagation speed, on the left and right of each window. This window length results in m_x =



128 elements that track the ISW as it shoals. As such, the total number of actively simulated degrees of freedom, at any given time, in 2D is 720×10^3 . The initial 2D simulation requires five windows while the ensuing 3D restart is covers nine windows. By using overlapping windows, simulating the remote wave upstream is avoided thereby reducing computational cost. The 3D simulation requires an adequate domain width that can allow for the lateral instability to form as the ISW shoals. The process of determining L_y was based on a series of test simulations that focused on capturing the emergence of the lateral instability.

The ISW-induced velocity and density field had to be slightly perturbed using a modified white noise sample to ensure that the 3D breaking process actually occurred, given that no self-excited 3D breaking mode has been reported in the literature for convectively unstable ISWs. A separate simulation (not shown) involving the present combination of the 143 m-amplitude initial wave with the observed background current and density profile without any noise insertion resulted in the absence of any 3D breaking.

To insert the noise field, first the wave-induced velocity and wave-induced density fields had to be extruded from 2D to 3D, in the y direction. The final noise sample field was obtained by first generating a white noise sample in a 3D undeformed domain with a mean of 0 and a variance of 1, then windowed along the lateral direction using a -5/3 power law in the Fourier domain. A maximum amplitude denoted by $\alpha_o = 10^{-6}$ m s⁻¹, taken to be a characteristic noise velocity, was utilized to scale the initial noise sample. The perturbed wave-induced velocity field is obtained from,

$$u'_{+} = u'_{-} + \alpha_{o}R$$

 $w'_{+} = w'_{-} + \alpha_{o}R,$ (8)

where R is the normally distributed field in 3D and, the plus and minus subscript corresponds to the perturbed and unperturbed 3D velocity fields, respectively. Similar to Fringer and Street [29], the transverse velocity field v' is determined from continuity after u' and w' have been perturbed. Note that the solution of the Pressure Poisson Equation in the SMPM code results in a solenoidal velocity field after one timestep [47].

The wave-induced density field was also perturbed using the same normally distributed noise sample field filtered along the lateral wavenumber in Fourier space, *R*. The perturbed wave-induced density field is obtained from,

$$\rho'_{+} = \rho'_{-} + \alpha'_{o}R, \tag{9}$$

where $\alpha'_o = 10^{-6} \text{ kg m}^{-3}$. Note that the wave-induced density field is of similar order of magnitude as the wave-induced velocity fields. Hereinafter the subscript $_+$ is dropped for convenience.

No strong transient response was noted between the velocity and density field as a result of including noise in the wave-induced density field. Noise insertion occurred at the beginning of the sixth window where the location of the wave was approximately 40 km into the shoaling transect (see Fig. 2). As soon as the simulation is initiated, the action of the spectral filter also ensures that the highest-resolved modes have very limited energy content.

After perturbing the wave-induced velocity and density field, the ISW then was allowed to propagate until the location of the deep mooring, where the field observations of Lien et al. [4] indicated that the flow inside the ISW should be 3D. The test simulations described earlier resulted in a dominant lateral wavelength of approximately 25 m. The value of L_{ν} was set to 50 m to accommodate two such wavelengths. Given that this value is



comparable to the size of the vertical overturn observed by Lien et al. [4], it may be reasonable to assume that the computational domain span for simulations of ISW with subsurface cores scales with the size of the overturns observed in the field.

Once the domain width was established, the 3D simulation was repeated but with an improved lateral resolution increasing m_y from 32 to 64. The same transverse modal structure was captured, indicating that the resulting resolution was adequate to capture the three-dimensionalization of the shoaling wave. The computational domain has total number of degrees of freedom in 3D of 576×10^6 but, with the windowing technique, only 46.08×10^6 are actively simulated, at any given time, using 128 cores per window. Note that the focus of the present study is to examine the transition from 2D to 3D of convective breaking, in terms of any 3D lateral instability and subsequent transition to turbulence, for this limited spanwise resolution. However, future 3D simulations will explore the turbulent aspect of the subsuface recirculating core at higher resolution in all three directions.

The timestep size, Δt , was specified so as to respect the Courant–Friedrichs–Lewy limit for the initial velocity scale and the grid properties; the limit was set to 0.50 for both the x and z direction and 0.25 in the y direction [48]. During the shoaling simulation, an adaptive timestepping method ensures that Δt is adjusted, if necessary; timestep adjustment would result from a change in the wave-induced velocity and propagation speed, or due to the small-scale features of the subsurface recirculating core. The initial timestep size was set to 0.2 s. Table 1 contains a summary of the grid properties for the present study.

3 Results

3.1 Visualizing the ISW at the moorings

Figure 3 shows density isosurfaces along with the lateral wave-induced velocity field, v', and the isopycnal structure above the pycnocline as the ISW approaches the deep mooring location. The wave trough is located at approximately x=53.6 km. In Fig. 3a, two isosurfaces are included to visualize the wave: the first isopycnal found to become convectively unstable in 2D, $\rho_c=1022.26$ kg m⁻³ (cyan), and the pycnocline, $\rho_o=1022.58$ kg m⁻³ (grey). The orange-dashed line denotes the 2D convective instability $U_{max}>c$, at an

Table 1 Grid properties for the simulations presented in this study

Parameter	Value	Parameter	Value
Δx_{\min}	1.121 m	Δx_{max}	6.945 m
$\Delta z_{min,deep}$	0.640 m	$\Delta z_{ m max, deep}$	3.967 m
$\Delta z_{\min, \text{sub}}$	0.314 m	$\Delta \mathbf{z}_{ ext{max,sub}}$	2.254 m
$\Delta z_{min,sur}$	0.296 m	$\Delta z_{ m max, sur}$	1.838 m
$\Delta z_{min,shallow}$	0.254 m	$\Delta z_{\rm max,shallow}$	1.578 m
$\Delta \mathbf{y}$	0.781 m	m _y	64
m _x	1600	m _z	25
n	15	$\Delta \mathbf{t}_{initial}$	0.2s

The regions included are: deep (i.e. 921 m), the deep (sub) and shallow (sur) mooring location, and shallow (i.e 360 m). Note that the Gauss-Lobatto-Legendre (GLL) grid is non-uniform locally in each SMPM element



approximate depth of 100 m, which is also shown in Fig. 3b. The black-dashed line corresponds to the location of the deep mooring. In Fig. 3c, a x–z plane transect of the ISW with the isopycnal structure above the pycnocline is shown. Here, the pycnocline is denoted as the grey-solid line. The x–z plane transect was extracted at approximately y = 25 m and, together with Fig. 2b, it shows a 2D evolution of the wave interior approaching the deep mooring location. In Fig. 3a and c, the arrow denotes the direction of propagation. Figure 3b, shows a x–y plane transect at a depth of 100 m with a contour of the lateral velocity. This variable is used to highlight the presence of the lateral instability that develops as the ISW shoals.

From Fig. 3, as the ISW approaches the deep mooring location, it becomes convectively unstable on the x-z plane, with the ρ_c isosurface overturning, and then the lateral instability begins to develop. The isopycnal structure shown in Fig. 3c appears to coincide with that shown by Rivera-Rosario et al. [24] in their Fig. 7b, albeit approximately 500 m before their wave location. Lateral variations in the density may be expected to occur at this location. However, Fig. 3b suggests that no such variations are present. Other than the modal structure of the lateral instability associated with a very weak velocity, no other 3D feature is evident. Additional simulations were performed with increased noise amplitude of up to $\alpha_o = 10^{-2}$ m s⁻¹ and $\alpha'_o = 10^{-2}$ kg m⁻³ for the wave-induced velocity and density, respectively, and these also exhibited convective breaking in 2D first. Note that the results of these additional simulations are not included in the present study. Thus, regardless of noise amplitude, 2D initial instability arises from the shoaling process and precedes any subsequent 3D lateral instabilities in contrast to what has been found in a 3D linear stability analysis for internal wave-critical layer interactions [49].

Figure 4 shows the ISW as it approaches the shallow mooring further along the propagation path from the deep mooring. The selected snapshots correspond to the following locations from left to right: 58.51 km (left), 60.03 km (middle), and 61.23 km (right). In addition to visualizing the convective overturning using isosurfaces, x–z and y–z plane transects are extracted to visualize the density; any overturns in the lateral direction may be easily discerned from the density field. The x–z plane transects shown in Fig. 4d–f corresponds to a span of approximately y = 25 m, and show the 2D evolution of the ISW, particularly the 2D convective instability initially shown in Fig. 3. The pycnocline is highlighted as the grey-solid line and the direction of wave propagation is noted by the black arrow. Figure 4g–i shows the plane transect in the y–z orientation with the density close to the wave trough. The red-line denotes regions of entrapped heavier fluid.

From Fig. 4a–c, it is apparent that the ISW is developing a lateral, 3D, structure in its interior. Examining the ρ_c isosurface suggests the presence of finer rib-like structures, similar to secondary instabilities in Kelvin–Helmholz billows [50]. Figure 4d–f shows that, as the ISW propagates past the shallow mooring, the heavier fluid intruding from behind the wave into the region above the trough has displaced the lighter fluid and eventually becomes trapped. This could be indicative of the presence of a subsurface recirculating core [24]. Figure 4g–i shows that the displaced light fluid rises, causing the formation of lateral convective instabilities. This lateral convective dynamic is initially shown in Fig. 4g. The convective instabilities drive the lateral structure of the flow, eventually resulting in finer scale vortical motion with components in the x–z direction that enhances energy dissipation and mixing, characteristic of a turbulent flow. Vorticity generation from the 2D wave-scale convective overturns has been studied in the context of breaking interfacial waves [27, 29], breaking internal waves in critical layers [26], and the breaking of internal gravity waves beneath critical layers [28].



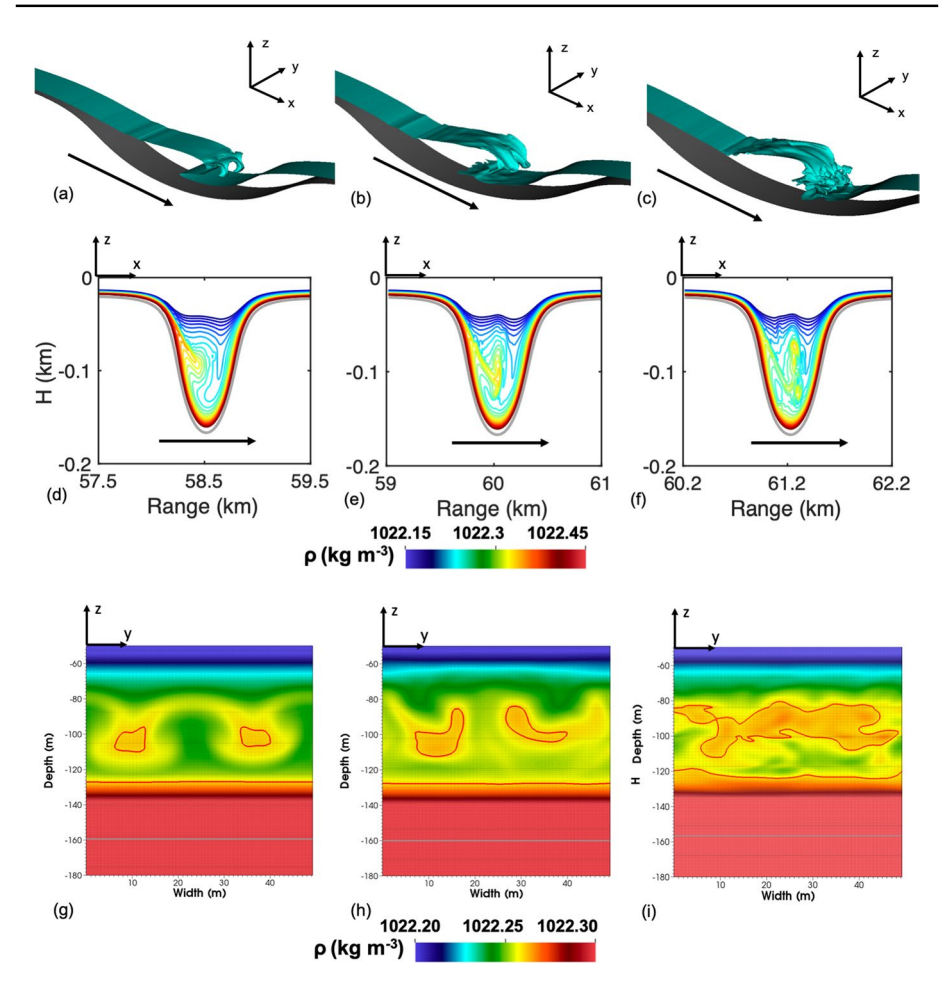


Fig. 4 The ISW along the shallow mooring location. The following locations are shown from left to right: 58.51 km , 60.03 km (shallow mooring), and 61.23 km. In **a–c** the isosurface values $\rho_c = 1022.26$ kg m⁻³ (cyan) and $\rho_o = 1022.58$ kg m⁻³ (grey) are shown. The black arrow indicates the direction of propagation. Panels **d–f** show a x–z plane transects at approximately y = 25 m, focused on the isopycnal structure above the pycnocline. Here, the pycnocline is denoted as the grey-solid line, and the arrow indicates the direction of propagation. Panels **g–i** show a y–z plane transect of total density close to the wave trough location, with the red-solid line used to highlight entrapped heavy fluid above the pycnocline, also denoted as the grey-solid line

The field observations of Lien et al. [4] indicate that, at the locations shown in Fig. 4, the ISW is expected be fully turbulent, with the subsurface core having already formed and being in the process of being transported onto shallower water. The present simulations appear to miss the timing of when the subsurface core is active, suggesting that, instead the ISW is in the process of transitioning from 2D to 3D with the core emerging shortly after (see Figs. 7 and 8 of Rivera-Rosario et al. [24]). It is suspected that the limited resolution combined with the filtering technique from the SMPM flow solver (see Sect. 2.2.2) is not adequate to capture the onset of small-scale instabilities that would result in an earlier 3D breaking.



3.2 ISW properties along the SCS bathymetric transect

The maximum ISW-induced velocity, U_{max} , propagation speed, c, amplitude, A, and width, L_w , can be computed and compared against field values to describe the simulated ISW as it shoals. In the present study, the ISW is tracked by locating the trough and, subsequently, the propagation speed is obtained by performing a least-squares fit using a linear model and computing the slope of the linear fit on sub-intervals of the position data [6, 24]. These sub-intervals cover a length of approximately one initial ISW-width. To account for the lateral dimension, each wave property is computed in the x-z plane and averaged along y. Uncertainty bounds have been calculated for the 3D simulation, nevertheless these were found to be minute (i.e. $< 10^{-2}$) and are not shown here.

Figure 5 shows the ISW properties, along with those from a 2D simulation, sampled until the wave reached the location of the moorings. In Fig. 5a–c, the properties of the 3D simulations are shown as the blue line and the properties of the 2D simulation as the black lines. The SCS bathymetric transect is shown in Fig. 5d as a reference, along with the locations of Figs. 2b, 3c, and 4d–f.

Notice that the 3D simulation exhibits similar values to those in the 2D simulations, since the curves in Fig. 5a–c mostly overlap, specially at the beginning where the 3D simulation is started in 2D. Considering the qualitative results shown in Fig. 4, the wave amplitude, width, and propagation speed are not indicators of any emerging lateral structure, that drives 3D breaking, since lateral effects appear to be confined to the region above the trough and will not necessarily reflect on the velocity and length scales, as computed through the process described at the beginning of this section.

Figure 6a shows the integrated kinetic energy components of the wave along the SCS transect (Fig. 6b). As the ISW shoals, the along-wave component increases while the

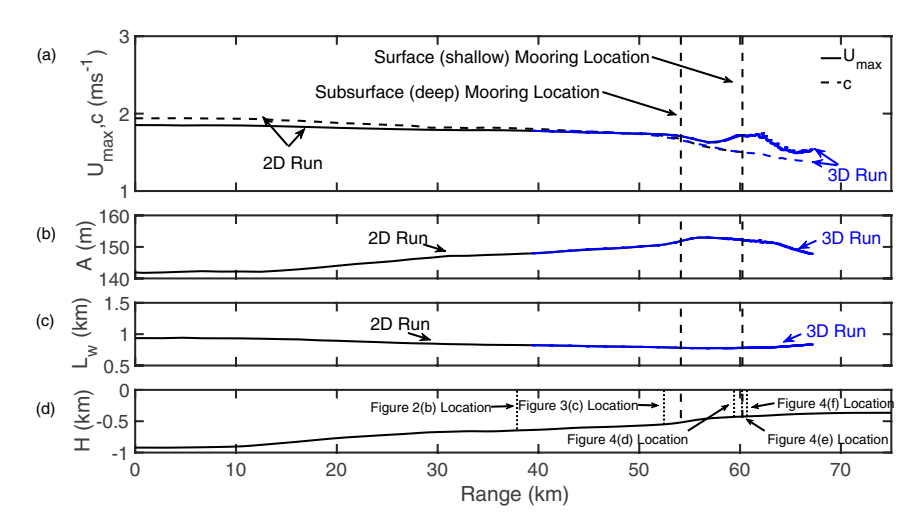


Fig. 5 Properties of the SCS shoaling simulation in 2D vs 3D. The properites of the 2D simulation are shown as the black lines. The properties of the 3D shoaling ISW are included as the blue lines; these are computed in every x–z plane and averaged in the lateral y direction. The wave properties include: maximum ISW-induced velocity, U_{max} , and propagation speed, c, in (a), ISW amplitude, A, in (b), and ISW halfwidth, L_w , in (c). The SCS bathymetric transect is included in (d) for reference, along with the locations of Figs. 2b, 3c, and 4d–f. In (a–d), the location of subsurface (deep) and surface (shallow) mooring is demarcated by the black-dashed lines in (a) through (d)



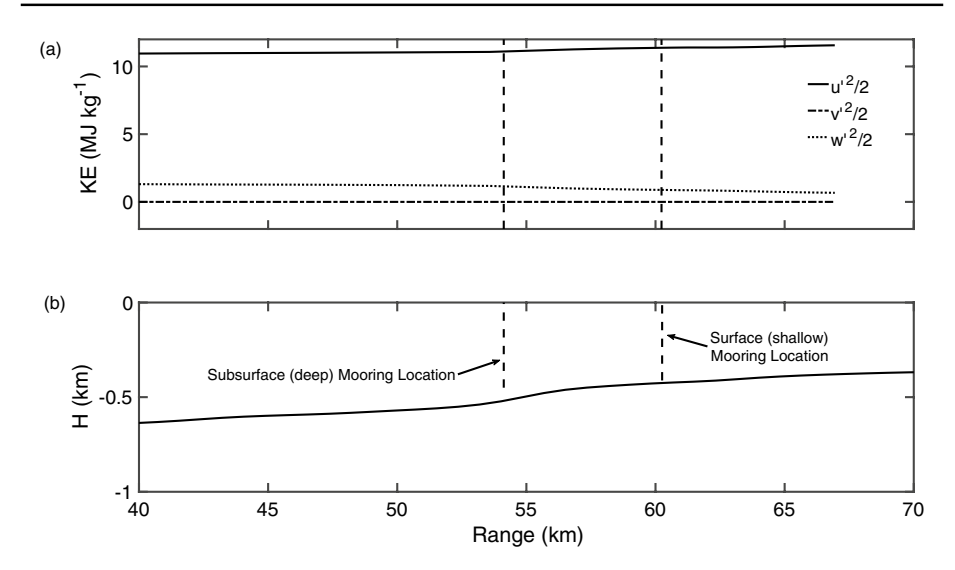


Fig. 6 Integrated kinetic energy components of the ISW along the bathymetric transect. The horizontal component $u'^2/2$, is denoted by the solid black line, the lateral component, $v'^2/2$, by the dashed-dotted line, and the vertical component, $w'^2/2$, by the dotted line. The SCS bathymetric transect is included in **b** for reference. The location of subsurface (deep) and surface (shallow) mooring is demarcated by the black-dashed lines in **a** and **b**

vertical component decreases; the lateral component remains significantly small. The maximum lateral value reaches approximately 10^{-4} MJ kg $^{-1}$ at the shallowest portion of the transect. The evolution of the components suggests that, eventhough the ISW breaking is in 3D, there is minimal energy from the 2D wave drained to excite 3D perturbations. The energy in the horizontal and vertical direction comes from the ISW itself.

Lastly, the simulated ISW propagation speed, maximum horizontal wave-induced velocity, and amplitude at the deep mooring were 1.66 m s⁻¹, 1.72 m s⁻¹, and 153 m, respectively. These values are very close to those reported by the 2D simulations of Rivera-Rosario et al. [24]. As noted by Rivera-Rosario et al. [24], differences between the observed and simulated wave are expected given that there is no observational input regarding the upstream conditions that would allow a more representative initial condition, and also since the upper 10 m of the background current profile was extrapolated.

3.3 Examining the lateral instability

The transition from 2D to 3D may be examined during shoaling by considering the energy content of the nondimensionalized Fourier coefficients of the wave-induced lateral velocity, $|a|c_{sub}^{-1}$, where c_{sub}^{-1} is the ISW speed at the subsurface (deep) mooring. Figure 7 shows the Fourier coefficients of the wave-induced lateral velocity as a function of the one-dimensional lateral wavenumber, K, computed by first generating a window in the x-z plane that is one ISW-width in length by 130 m in height, sufficient to encompass the convectively unstable region above the trough where the lateral instability develops (see Fig. 3). Subsequently, the resulting y-averaged spectra were averaged in x and z. The colored lines plotted in Fig. 7 correspond to selected locations between the deep (blue) and shallow (red)



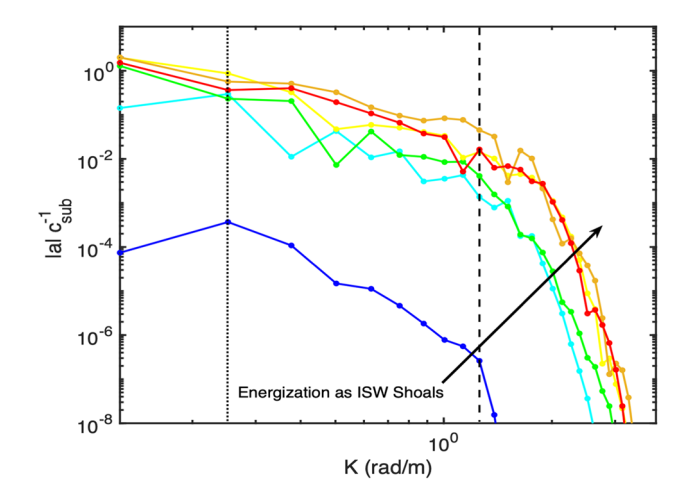


Fig. 7 Spatial evolution of the transverse Fourier coefficients of the wave-induced lateral velocity, v', obtained from a portion of the simulation window encompassing the convectively unstable region above the trough where the lateral instability develops. The coefficients are nondimensionalized by the wave speed at the subsurface (deep) mooring, c_{sub} . Each colored solid line corresponds to a simulation output located between the deep (blue) and shallow (red) mooring, along the SCS transect. The dotted line corresponds to the wavenumber of the lateral instability shown in the x-y plane in Fig. 3b. The dashed line indicates the first wavenumber where the spectral filter acts [42]. The arrow denotes the portion of the spectra that becomes energized as the ISW shoals

mooring. The dotted line corresponds to the wavenumber of the lateral instability shown in the x–y plane in Fig. 3b and the dashed line represents the value of the lateral Fourier wavenumber at which the transfer function of the exponential filter departs from unity. This wavenumber corresponds to a length scale of approximately 5 m. Lastly, the arrow denotes the direction in which the spectra develops in time as the ISW shoals.

From Fig. 7, as the ISW propagated over the deep mooring, most of the energy is confined to the smallest wavenumbers. However, by the time the ISW reaches the shallow mooring location, the highest wavenumbers begin to energize. Note that regardless of location, the sudden drop at high wavenumbers is due to the action of the exponential filter [42]; it begins to act approximately on the 20th wavenumber, i.e. where the filter function begins to departs from unity (see Fig. 2 of Diamessis et al. [46]). The latter wavenumber corresponds to a length scale of approximately 4.99 m. The present study suggests that the ISW may be in the process of becoming turbulent as it approaches the shallow mooring location, significantly delayed when compared to the field observations of Lien et al. [4].

Lastly, from the spectra showed in Fig. 7, as the wave shoals the small wavenumbers also increase in energy content. An increase in ISW amplitude is expected during shoaling since kinetic energy is converted to Available Potential Energy (APE) [51], and it may be possible that the presence of the baroclinic background current is contributing to the APE growth and ultimately energizing the small wavenumbers since the current is frozen. Unfortunately, the present simulation setup precludes an energy budget analysis [52] that could corroborate the impact of the background current in the wave energy transfer during shoaling due to the



limited resolution. Future work, equipped with enhanced resolution [53], will focus on computing the turbulent properties of the wave including more detailed energetics.

4 Conclusion

The shoaling of an ISW of depression over a gentle slope has been examined via high accuracy/resolution 3D numerical simulations that have incorporated realistic bathymetry and measured field conditions. The numerical approach involves solving the incompressible Navier–Stokes Equations under the Boussinesq approximation in 2D and 3D, using a high-order spectral multidomain penalty method (SMPM) flow solver. The bathymetry, density, and background current fields, used to generate the initial conditions, were obtained from the work of Lien et al. [4], and correspond to the water column properties in the South China Sea (SCS) on June 2, 2011. The wave propagates normal to the isobaths, yet a 3D structure can develop inside the wave itself.

The present study has built on the simulations of Rivera-Rosario et al. [24] by incorporating their initial ISW, as obtained from the solution of the Dubreil–Jacotin–Long (DJL) equation [33] with the observed density and background current field. In addition, the computational grid in the present study has the same vertical resolution but has double the resolution in the horizontal, and incorporates a lateral dimension with equidistant points. A series of test simulations were carried out to determine the appropriate computational domain width, with the value being 50 m, comparable to the size of the overturns observed in the field for ISWs of depression with a subsurface recirculating core [3, 4].

The simulated ISW is initially 2D and propagates along the SCS bathymetry for over 40 km, prior to the location where it would become convectively unstable according to the study of Rivera-Rosario et al. [24]. Here, the simulation is restarted in 3D by extruding the computational domain, with noise inserted in the wave-induced velocity and density fields to ensure that 3D breaking would eventually occur as the ISW propagates towards shallower water. Test simulations have demonstrated that without any noise insertion the rest of the shoaling process remains 2D.

The location of the subsurface (deep) and surface (shallow) moorings deployed by Lien et al. [4] is used to guide the analysis of the present study. The computed wave amplitude, width, and propagation speed are very close to those from the 2D study of Rivera-Rosario et al. [24]. Visualization of the isosurfaces and isopycnals above the pycnocline, along with lateral wave-induced velocity, v', indicate the presence of a lateral instability, as the ISW arrives at the deep mooring location (see Fig. 4). Overturning clearly precedes any lateral structure development. Visual confirmation of 3D breaking is established on the x–z plane once the wave reaches the shallow mooring location and not before as expected from the field observations. More simulations could be carried by varying the initial noise amplitude but, it is suspected that the limited resolution combined with the filtering technique from the SMPM flow solver is not adequate to capture the small-scale turbulence responsible for exciting any instabilities that would result in earlier 3D breaking.

The SMPM flow solver demonstrated that it can simulate the shoaling ISW of depression over gentle slopes, in 2D and 3D, and capture the initial 2D convective instability. The observations used to drive the simulations were obtained during field expeditions focused on examining the convectively unstable ISW and the formation of a subsurface recirculating core in the SCS [3, 4]. As such, it may be possible to utilize this numerical tool to examine ISW propagation in other oceanic environments such as the Northwestern



Australian continental shelf [54], the Washington continental shelf [55], or the New Jersey continental shelf [13, 16], and highlight the presence of convective instability and potential core formation, specially where high-resolution field data of the water column properties and bathymetry are available.

Future studies will examine the turbulent properties of the 3D breaking wave and the subsurface recirculating core that forms after the convective instability. Such higher-resolution studies would focus on characterizing the turbulence that forms during the 3D convective breaking process and then develops within the subsurface core. Particular emphasis would be placed on visualizing the turbulent flow structure, computing ISW energetics and monitoring in greater detail the evolution of the marginal convective instability (proposed by Chang et al. [2]) over the full wave propagation path. A highly accurate particle tracking technique [56] will be incorporated to examine the properties of the core from a Lagrangian perspective. The method can also provide a quantification of the recirculating core mass transport, as the ISW shoals over gentle slopes.

Acknowledgements The authors would like to thank Theodoros Diamantopoulos, Marek Stastna, Yangxin He, and Frank Henyey for their insightful comments and suggestions regarding recirculating cores and this work. Financial support is gratefully acknowledged from National Science Foundation—Division of Ocean Sciences (OCE) Grant 1634257.

Declarations

Conflict of interest The authors declare that they have no conflict of interest.

References

- Chang MH, Cheng YH, Yang YJ, Jan S, Ramp SR, Reeder DB, Hsieh WT, Ko DS, Davis KA, Shao HJ, Tseng RS (2021) Direct measurements reveal instabilities and turbulence within large amplitude internal solitary waves beneath the ocean. Commun Earth Environ 2(1):15. https://doi.org/10.1038/ s43247-020-00083-6
- Chang MH, Lien RC, Lamb K, Diamessis P (2021) Long-term observations of shoaling internal solitary waves in the northern South China Sea. J Geophys Res Oceans. https://doi.org/10.1029/2020JC017129
- Lien RC, D'Asaro E, Henyey F, Chang MH, Tang TY, Yang YJ (2012) Trapped core formation within a shoaling nonlinear internal wave. J Phys Oceanogr 42:511–525
- Lien RC, Henyey F, Ma B, Yang YJ (2014) Large-amplitude internal solitary waves observed in the northern South China Sea: properties and energetics. J Phys Oceanogr 44(4):1095–1115. https://doi. org/10.1175/JPO-D-13-088.1
- Moum J, Farmer D, Smyth W, Armi L, Vagle S (2003) Structure and generation of turbulence at interfaces strained by internal solitary waves propagating shoreward over the continental shelf. J Phys Oceanogr 33:2093–2112
- Moore S, Lien RC (2007) Pilot whales follow internal solitary waves in the South China Sea. Mar Mammal Sci 21(1):193–196
- Bogucki D, Redekopp L (1999) A mechanism for sediment resuspension by internal solitary waves. Geophys Res Lett 26(9):1317–1320
- Diamessis P, Redekopp L (2006) Numerical investigation of solitary internal wave-induced global instability in a shallow water benthic boundary layers. J Phys Oceanogr 36:784–812
- Sakai T, Diamessis PJ, Jacobs GB (2020) Self-sustained instability, transition, and turbulence induced by a long separation bubble in the footprint of an internal solitary wave. I. Flow topology. Phys Rev Fluids 5:103801. https://doi.org/10.1103/PhysRevFluids.5.103801
- Sakai T, Diamessis PJ, Jacobs GB (2020) Self-sustained instability, transition, and turbulence induced by a long separation bubble in the footprint of an internal solitary wave. II. Flow statistics. Phys Rev Fluids 5:103802. https://doi.org/10.1103/PhysRevFluids.5.103802



- Stastna M, Lamb K (2008) Sediment resuspension mechanism associated with internal waves in coastal waters. J Geophys Res. https://doi.org/10.1029/2007JC004711Citations
- Zulberti A, Jones NL, Ivey GN (2020) Observations of enhanced sediment transport by nonlinear internal waves. Geophys Res Lett. https://doi.org/10.1029/2020GL088499
- Shroyer EL, Moum JN, Nash JD (2010) Energy transformations and dissipation of nonlinear internal waves over New Jersey's continental shelf. Nonlinear Process Geophys 17(4):345–360. https:// doi.org/10.5194/npg-17-345-2010
- St Laurent L (2008) Turbulent dissipation on the margins of the South China Sea. Geophys Res Lett. https://doi.org/10.1029/2008GL035520
- St Laurent L, Simmons H, Tang TY, Wang Y (2011) Turbulent properties of internal waves in the South China Sea. Oceanography. https://doi.org/10.5670/oceanog.2011.96
- Shroyer EL, Moum JN, Nash JD (2010) Vertical heat flux and lateral mass transport in nonlinear internal waves. Geophys Res Lett. https://doi.org/10.1029/2010GL042715
- Vlasenko V, Ostrovsky L, Hutter K (2005) Adiabatic behavior of strongly nonlinear internal solitary waves in slope-shelf areas. J Geophys Res. https://doi.org/10.1029/2004JC002705
- 18. Aigner A, Broutman D, Grimshaw R (1999) Numerical simulations of internal solitary waves with vortex cores. Fluid Dyn Res 25:315–333
- 19. Derzho O, Grimshaw R (1997) Solitary waves with a vortex core in a shallow layer of stratified fluid. Phys Fluids 9(11):3378–3785
- Lamb K (2002) A numerical investigation of solitary internal waves with trapped cores formed via shoaling. J Fluid Mech 451:109–144
- Lamb K (2003) Shoaling solitary internal waves: on a criterion for the formation of waves with trapped cores. J Fluid Mech 478:81–100
- Choi W (2006) The effect of a background shear current on large amplitude internal solitary waves. Phys Fluids 18:036601
- 23. He Y, Lamb K, Lien RC (2019) Internal solitary waves with subsurface cores. J Fluid Mech 873:1-17
- Rivera-Rosario G, Diamessis PJ, Lien RC, Lamb KG, Thomsen GN (2020) Formation of recirculating cores in convectively breaking internal solitary waves of depression shoaling over gentle slopes in the South China Sea. J Phys Oceanogr 50(5):1137–1157. https://doi.org/10.1175/JPO-D-19-0036.1
- Andreassen O, Easber C (1994) Gravity wave breaking in two and three dimensions: 1. Model description and comparison of two-dimensional evolutions. J Geophys Res 99(D4):8095–8108
- Winters K, D'Asaro E (1994) Three-dimensional wave instability near a critical layer. J Fluid Mech 272:255–284
- Arthur R, Fringer O (2014) The dynamics of breaking internal solitary waves on slopes. J Fluid Mech 761:360–398
- 28. Dörnbrack A (1998) Turbulent mixing by breaking gravity waves. J Fluid Mech 375:113-141
- Fringer O, Street R (2003) The dynamics of breaking progressive interfacial waves. J Fluid Mech 494:319–353
- Diamessis P, Domaradzki J, Hesthaven J (2005) A spectral multidomain penalty method model for the simulation of high Reynolds number localized incompressible stratified turbulence. J Comput Phys 202:198–322
- Joshi S (2016) Development of fast high-order numerical methods for high-Reynolds number environmental flows. PhD thesis, Cornell University
- 32. Boyd J (2001) Chebyshev and Fourier spectral methods, 2nd edn. Dover Publications Inc., Mineola
- Dunphy M, Subich C, Stastna M (2011) Spectral methods for internal waves: indistinguishable density profiles and double-humped solitary waves. Nonlinear Process Geophys 18:351–358
- Koop G, Butler G (1981) An investigation of internal solitary waves in a two-fluid system. J Fluid Mech 112:225–251. https://doi.org/10.1017/S0022112081000372
- Joshi S, Thomsen G, Diamessis P (2016) Deflation-accelerated preconditioning of the Poisson— Neumann Schur problem on long domains with a high-order discontinuous element-based collocation method. J Comput Phys 313:209–232
- Kopriva D (2009) Implementing spectral methods for partial differential equations. Springer, Dordrecht
- 37. Kundu P, Cohen I, Dowling D (2012) Fluid mechanics. Elsevier, Amsterdam
- Lamb K, Warn-Varnas A (2015) Two-dimensional numerical simulations of shoaling internal solitary waves at the ASIAEX site in the South China Sea. Nonlinear Process Geophys 22:289–312
- 39. Helfrich K, Melville W (2006) Long nonlinear internal waves. Annu Rev Fluid Mech 38:395-425
- Karniadakis G, Israeli M, Orszag S (1991) High-order splitting methods for the incompressible Navier–Stokes equations. J Comput Phys 97:411–443



- 41. Abdilghanie A (2011) A numerical investigation of turbulence-driven and forced generation of internal gravity waves in stratified mid-water. PhD thesis, Cornell University
- Blackburn H, Schmidt S (2003) Spectral element filtering techniques for large eddy simulation with dynamic estimation. J Comput Phys 186:610–629
- Escobar-Vargas J, Diamessis P, Sakai T (2014) A spectral quadrilateral multidomain penalty method model for high Reynolds number incompressible stratified flows. Int J Numer Methods Fluids 75:403–425
- Long R (1953) Some aspects of the flow of stratified fluids: I. A theoretical investigation. Tellus 8:460–471
- 45. Turkington B, Eydeland A, Wang S (1991) A computational method for solitary internal waves in a continuously stratified fluid. Stud Appl Math 85:93–127
- Diamessis P, Lin Y, Domaradzki J (2008) Effective numerical viscosity in spectral multidomain penalty method-based simulations of localized turbulence. J Comput Phys 227:8145

 –8164
- Joshi S, Diamessis P, Steinmoller D, Stastna M, Thomsen G (2016) A post-processing technique for stabilizing the discontinuous pressure projection operator in marginally-resolved incompressible inviscid flow. Comput Fluids 139:120–129
- 48. Canuto C, Hussaini M, Quarteroni A, Zang T (2006) Spectral methods fundamentals in single domains. Springer, Berlin
- Winters KB, Riley JJ (1992) Instability of internal waves near a critical level. Dyn Atmos Oceans 16:249–278
- Brown GL, Roshko A (1974) On the density effects and large structure in turbulent mixing layers. J Fluid Mech 64:775–816
- Lamb K, Nguyen V (2009) Calculating energy flux in internal solitary waves with an application to reflectance. J Phys Oceanogr 39:559–580
- Winters K, Lombard P, Riley J, D'Asaro E (1995) Available potential energy and mixing in densitystratified fluids. J Fluid Mech 289:115–128
- 53. Diamantopoulos T (2021) A high-order hybrid flow solver for the simulation of non-linear internal waves in long complex domains: exploring the turbulent aspects of a recirculating core in a shoaling internal solitary wave of depression. PhD thesis, Cornell University
- 54. Holloway P (1987) Internal hydraulic jumps and solitons at a shelf break region on the australian north west shelf. J Geophys Res 92(C2):5405–5416
- Zhang S, Alford M (2015) Instabilities in nonlinear internal waves on the Washington continental shelf. J Geophys Res 120:5272–5283
- Klose BF, Jacobs GB, Serra M (2020) Kinematics of Lagrangian flow separation in external aerodynamics. AIAA J 58(5):1926–1938. https://doi.org/10.2514/1.J059026

Publisher's Note Springer Nature remains neutral with regard to jurisdictional claims in published maps and institutional affiliations

